Computational Modeling of Polycrystalline Silicon on Oxide Passivating Contact for Silicon Solar Cells

Rehan Younas, Hassan Imran, Syed Ijlal Hassan Shah, Tarek M. Abdolkader, *Member, IEEE*, and Nauman Zafar Butt, *Member, IEEE*

***Abstract*— Polycrystalline silicon on oxide (POLO) junction passivating contacts have recently been demonstrated as carrier selective contacts for high-efficiency silicon solar cells. The carrier transport through these contacts has been attributed to two competing mechanisms: 1) carrier tunneling through ultrathin oxide and 2) transport through weak spots (pinholes) – the nanoscale regions where oxide thickness has been completely or partially compromised during the processing. In this paper, we use two dimensional device simulations to compare the relative effects of these mechanisms on solar cell characteristics with n-type POLO contact. We show that variation in pinhole areal density (D_{ph}) or the tunnel oxide thickness (t_{ox}) both result in qualitatively similar trends in the cell characteristics under dark and light. For a given t_{ox}, an exponential variation in D_{ph} results in trends that are similar to those for a linear variation in t_{ox}. The effect of pinholes on contact resistance (ρ_c) and saturation current density (J_o) is most significant for relatively thicker oxides ($\geq$ 2 nm). For $t_{ox} \leq$ 1 nm, ρ_c and J_o become essentially insensitive to pinholes for $D_{ph} < 10^{10}$ cm^{-2}. The modeling results are compared with a set of published experimental data to predict the possible roles of various mechanisms.**

***Index Terms*— Contact resistance, pinhole, saturation current density, tunneling.**

I. Introduction

CARRIER selectivity is one of the key requirements to achieve efficiency of solar cells closer to the maximum limit of 29.5% [1]. Carrier selective contacts favor the flow of majority carriers and prevent the flow of minority carriers thus reducing the undesired recombination at the metal contacts. The classical example of a carrier selective contact is the well-known heterojunction with intrinsic thin layer silicon solar cell in which a thin layer of amorphous silicon (a-Si) makes a heterojunction with crystalline silicon (c-Si) base that can provide an excellent surface passivation and high efficiency (26.7%) [2]. However, the low thermal stability and parasitic absorption losses due to lower bandgap of a-Si [3], [4] have motivated research on alternative technologies [5], [6].

A set of alternative carrier selective contacts for silicon heterojunction are being investigated including transition metal oxides such as molybdenum oxide (MoO_x), nickel oxide (NiO_x) for p-type, titanium dioxide (TiO_2), and zinc oxide (ZnO) for n-type contacts [7]–[10]. They offer reasonable thermal stability, better transparency due to their higher bandgaps (>3 eV), and require low-temperature fabrication. Various organic materials have also been demonstrated to improve carrier selectivity such as naphthalene-based polymer P(NDI2OD-T2) acting as an electron contact and polythiophenes being hole selective contact [11], [12]. While these metal oxide and organic material-based contacts have demonstrated high potential for carrier selectivity, they are still under development to be incorporated within current c-Si photovoltaic technology.

Building upon the concept of polycrystalline silicon (poly-Si) emitters for bipolar transistors [13]–[16], carrier selective contacts for c-Si-based solar cells have been demonstrated using poly-Si in place of using a-Si to avoid high-temperature stability issues [17]–[19]. Lindholm *et al.* [17] first introduced the concept of poly-Si based carrier selective contact that showed improvement in red spectral response and promised high value of open circuit voltage (V_{oc}). However, the surface defects due to lattice mismatch issue at the poly-Si/c-Si junction limited its use. Gan and Swanson [18] investigated the role of thin SiO_2 layer at poly-Si/c-Si junction and discussed the effects of oxide break-up.

Working on this concept of polycrystalline silicon on oxide (POLO) junction, a number of studies have explored the concept of full area covered passivating contacts [19]–[23]. The main benefit of adding this layer of oxide between c-Si base and poly-Si is the suppression of minority carrier recombination at the contact. For example, Rohatgi *et al.* [22] report solar cells with 1.5-nm-thick oxide layer exhibiting excellent passivation ($J_o \sim 5$ fA/cm^2) and very low values of contact resistance ($\rho_c \sim 7$ mΩcm^2). While these POLO solar

Manuscript received November 11, 2018; revised January 10, 2019 and February 11, 2019; accepted February 18, 2019. Date of publication March 6, 2019; date of current version March 22, 2019. The review of this paper was arranged by Editor B. Hoex. *(Corresponding author: Rehan Younas.)*

R. Younas, H. Imran, S. I. H. Shah, and N. Z. Butt are with the Department of Electrical Engineering, Syed Babar Ali School of Science and Engineering, Lahore University of Management Sciences, Lahore 54792, Pakistan (e-mail: reh.younas@gmail.com; hassan.imran.ee@gmail.com; ijlalhassah@yahoo.com; nauman.butt@lums.edu.pk).

T. M. Abdolkader is with the Department of Electrical Engineering, Umm Al-Qura University, Makkah 13174, Saudi Arabia (e-mail: tmhasan@uqu.edu.sa).

Color versions of one or more of the figures in this paper are available online at http://ieeexplore.ieee.org.

Digital Object Identifier 10.1109/TED.2019.2900691

cells can provide excellent values of V_{oc} and fill factor (FF), their underlying charge carrier transport mechanism is still under debate in the literature. Originally, it was thought that the quantum mechanical tunneling through the oxide layer is the sole mechanism dominating the carrier transport [13], [24], [25]. The experimental data from different groups, however, exhibited quite a large variation in trends which has led some researchers proposing alternative transport mechanisms [26]–[30]. For example, data of Gan and Swanson show excellent values of contact resistance but with relatively higher values of saturation current [18]. This may seem surprising particularly for the fact that Gan has used presumably thicker oxide layer ($t_{ox} > 2$ nm) for which the tunneling through oxide should not be very strong. On the contrary, the data of Peibst *et al.* show higher values of contact resistance ($\rho_c \sim 100$ mΩcm^2) and very low values of saturation current ($J_o \sim 1$ fA/cm^2) while using relatively thin oxide ($t_{ox} < 2$ nm) [26], [31]–[33]. A fundamental reason for Peibst *et al.* [26] to question the standard tunneling model was the observation of symmetrical electrical behavior for symmetrically (n-Si/n-poly) and asymmetrically (n-Si/p-Si) doped contacts despite unequal tunneling barrier height for electrons and holes. Similar variations in the reported experimental data have stimulated interest in an in-depth analysis of POLO contacts where some research has proposed the transport through pinholes (nanoscale spots of localized reduction in the interfacial oxide layer) as an alternative mechanism to the tunneling [30], [34]. For example, Gan and Swanson [18] attributed the low contact resistance values observed for $t_{ox} > 2$ nm in their experimental data to pinholes. Wietler *et al.* [35] also report an excellent match of measured and predicted values of J_o and ρ_c for pinhole mediated charge carrier transport in their samples. Various analytical and numerical models have also been presented to explain the trends observed in the experimental data using tunneling or pinhole models [22], [25], [36]–[38]. Peibst *et al.* [26], [33], [35], for example, have developed an analytical model based on carrier transport through pinholes. A recent work by Feldmann [39], [40] on the selective etching and temperature-dependent $J - V$ measurements and similar work by Folchert provide an estimation of the fraction of tunnel and pinhole transport based on sample characterization [41]. Although these previous studies provide important insights, there is, however, no numerical modeling work so far which incorporates both mechanisms simultaneously and study their relative effects on cell characteristics under dark and illumination. A study based on self-consistent device simulations, in particular, is needed to incorporate the coupled effects of current crowding and surface band bending at the POLO contacts.

The objective of this paper is to use self-consistent 2-D numerical device simulations to quantify the relative effects of tunneling and pinholes on POLO solar cell characteristics. The modeling results are then compared with a set of published experimental data to understand the mechanisms underlying the experimental trends. It is of importance to mention here that although transport through pinholes ideally requires a 3-D model, 2-D approach used here is still valuable and could be used to infer first-order insights into the trends in the experimental data.

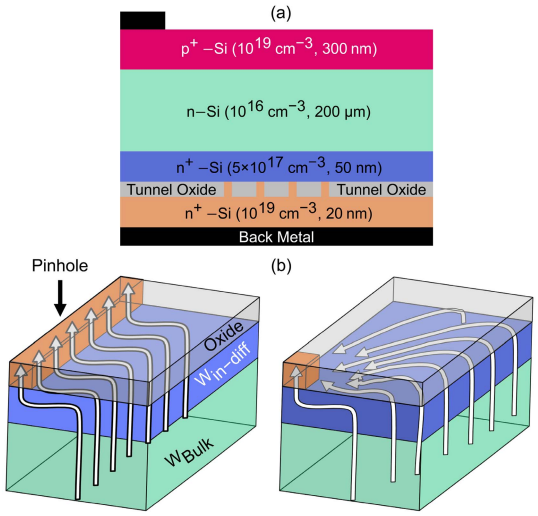

Fig. 1. (a) 2-D schematic of the solar cell modeled in this paper. The pinholes are distributed uniformly across the POLO interface. (b) 3-D illustration of current paths for a line versus point contact.

We divide this paper into four sections. Section II describes the modeling approach. Section III discusses the results, and conclusions are provided in Section IV.

II. Modeling Approach

A 2-D schematic of the solar cell is shown in Fig. 1(a). The cell structure consists of n-doped crystalline silicon (c-Si) as the photoabsorbing material. A thin layer of p^+ c-Si is used at the top as an emitter. At rear, we have POLO interface that consists of an ultrathin oxide stacked on a highly doped polycrystalline silicon (poly-Si) layer of 20 nm thickness. A shallow region of 50 nm with doping concentration of 5×10^{17} cm^{-3} is assumed to be formed underneath the oxide layer in c-Si bulk to account for the dopant in-diffusion as reported in [26] and [39]–[41]. Front is partially contacted with nickel (work function (ϕ_M) = 5.1 eV) to let sunlight pass through while back is fully covered with aluminum ($\phi_M = 4.1$ eV) contact. Surface recombination velocity (v_{surf}) at the front contact is 1 cm/s while at back is 10^7 cm/s unless otherwise specified. Other parameters used for simulations of the cell are listed in Table I.

Pinholes have been modeled by poly-Si tunnels through the oxide with a single pinhole having surface area of 4 nm^2. Fig. 1(b) shows an illustration of current paths and the effective geometry of a single pinhole in our simple 2-D model (line contact) with a comparison to a more realistic 3-D (point contact) scenario. A difference in the lateral current paths and crowding effect may result in a quantitative error in our simulated ρ_c and J_o. We investigate this by comparing our simulated ρ_c and J_o with that obtained through well-known Fischer's model [42] for point contacts (see Appendix D). The simulated ρ_c is subsequently scaled with a constant correction factor for all simulation results while a good quantitative match was found for J_o. As our 2-D model is implicitly symmetric

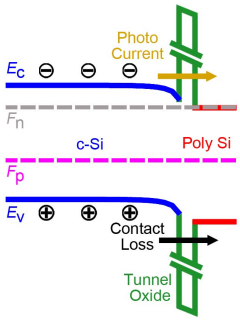

Fig. 2. Energy band diagram of n-type POLO contact under short circuit condition with direction of tunneling highlighted. The diagram is not drawn to the scale.

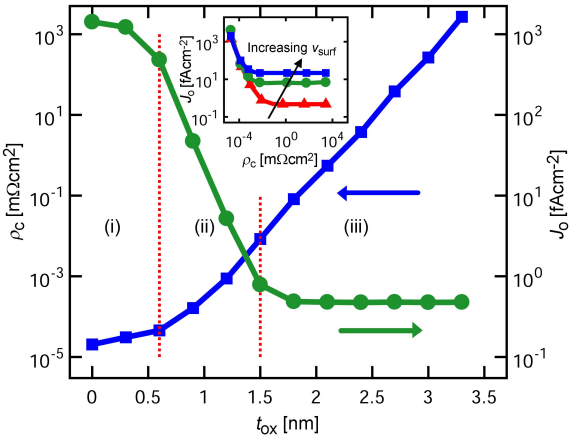

Fig. 3. Trend of J_o and ρ_c as a function of t_{ox} is presented keeping v_{surf} (1 cm/s) at the front contact. Inset shows the trend of J_o versus ρ_c for which v_{surf} is varied from 1 cm/s to 100 cm/s and 400 cm/s.

in the 3rd dimension, the linewidth of pinhole is reduced to match the surface area with that of 3-D.

We consider two situations for the resistance of pinholes: the first case is when pinhole breaks the oxide completely and poly-Si comes in direct contact with c-Si (shorted pinhole), and the second case is when some residual oxide is still intact in the pinhole region (resistive pinhole). For our model, we consider this residual oxide in the range of 0.1 – 0.6 nm. The pinhole areal density (D_{ph}) is varied in the range of $\sim 10^7$ – 10^{11} cm^{-2}.

The effect of interfacial defects (D_{it}) is modeled through v_{surf}. The interfacial defect density could be analytically expressed as [43]:

$$D_{it} = \frac{v_{surf}}{\sigma v_{th} \Delta E} \tag{1}$$

where σ is the capture cross section and is assumed equal to 1×10^{-15} cm^{-2} [44], and v_{th} is the carrier thermal velocity $\sim 10^7$ cm/s for c-Si. The interfacial defects are assumed to be spread uniformly throughout the energy range (ΔE), which is assumed to be equal to the bandgap of silicon.

A. Cell Electrostatics/Carrier Transport

The energy band diagram of the cell under short-circuit condition is shown in Fig. 2. The photogeneration of carriers takes place inside c-Si and drift-diffusion flux of these carriers move towards their respective contacts. At the semiconductor/oxide interface, charge carriers can either tunnel or jump over the energy barrier through thermionic emission. Since the energy barrier offered by the oxide layer is very high, i.e., 3.2 eV for electrons and 4.6 eV for holes [45], the probability of thermionic emission is significantly suppressed. The dominant mechanism for current flow is, therefore, tunneling through oxide, conduction through pinholes, and/or recombination due to interfacial states. The device simulations are done in PADRE which is a 2-D simulator designed to numerically solve the coupled set of carrier continuity equations and the Poisson equation self-consistently [46].

Since PADRE does not provide a direct model for quantum mechanical tunneling, we use a two-step approach to implement it at the POLO contact. First, we calculate the tunneling probability (T_{QM}) at the contact using rigorous quantum mechanical simulations. Next, a phenomenological approach is used to implement T_{QM} in PADRE by making adjustment in the thermionic barriers for electrons and holes at the POLO contact. For the 1st step, we use Transfer Matrix Method (TMM) that numerically solves the Schrödinger equation through the thin oxide barriers at the contact. The details of this method have been reported elsewhere [7], [47]. Comparing TMM with the conventional finite difference method commonly used for numerically solving the Schrödinger equation, it has been shown that TMM provides a better accuracy [48]. Fig. A1 shows T_{QM} for electrons at POLO contact and a comparison with an analytical approach based on W-K-B approximation. An equivalent probability for thermionic emission (T_{therm}) for a given t_{ox} could be calculated by:

$$T_{therm} = T_{QM} = e^{-\phi_{n(p),eff}/k_B T} \tag{2}$$

where $\phi_{n(p),eff}$ is the effective thermionic barrier for electrons (holes), T is the temperature, and k_B is Boltzmann's constant. The calculated $\phi_{n(p),eff}$ are then incorporated in PADRE by adjusting the effective electron affinity (χ) and bandgap (E_g) of the oxide layer. It is straightforward to show that this phenomenological approach preserves the surface band bending while effectively modeling the quantum tunneling at the POLO contact (see Appendix B). The procedure for extraction of J_o and ρ_c is discussed in Appendix C.

III. Results and Discussion

A. Trends Under Dark

The essential figures of merit for an efficient solar cell contact include contact resistance and saturation current density. Fig. 3 shows the trend of ρ_c and J_o as a function of t_{ox} variation. The observed behavior can be classified into three regions. First, the region in which ρ_c shows a relatively small change with t_{ox} variation (region (i) in Fig. 3). This is the regime of ultrathin oxide layer ($t_{ox} \leq 0.6$ nm). Since tunneling probability is very strong in this regime, the oxide remains relatively transparent to both majority and minority carrier and the substrate properties are significant for both J_o and ρ_c. In the second region, ρ_c (J_o) increases (decreases) with increasing t_{ox} (region (ii) in Fig. 3). This is the region

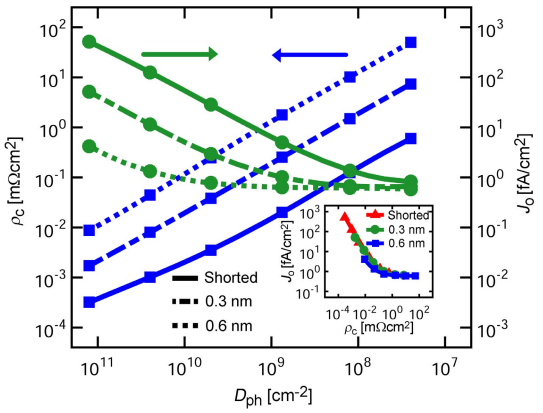

Fig. 4. J_o and ρ_c trends as a function of D_{ph} for $t_{ox} = 3$ nm and three different cases of: 1) shorted pinholes, 2) moderately resistive pinhole with 0.3-nm residual oxide; and 3) highly resistive pinhole with 0.6-nm residual oxide. Inset shows J_o versus ρ_c trends for three different cases of pinholes.

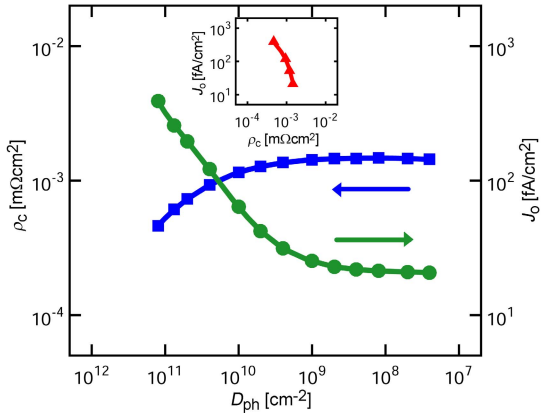

Fig. 5. J_o and ρ_c as a function of D_{ph} for a thin oxide layer ($t_{ox} = 1$ nm). In this case, shorted pinholes are considered.

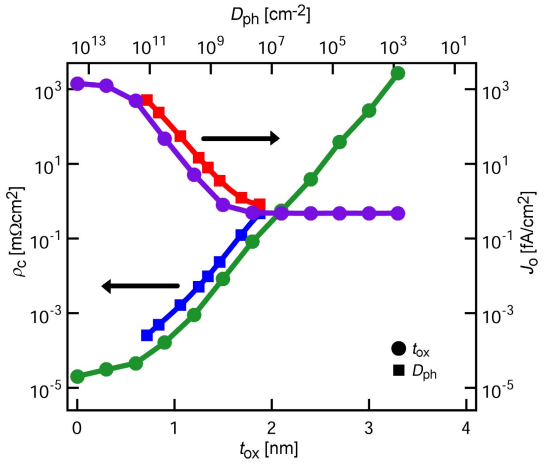

Fig. 6. Comparison of trends for J_o and ρ_c as a function of t_{ox} and D_{ph}. In this case, shorted pinholes formed in a 3-nm-thick oxide have been assumed.

of moderate oxide thickness ($0.6 \leq t_{ox} \leq 1.5$ nm) which is strongly sensitive to t_{ox} while the substrate properties play a negligible role here. Third is the region in which J_o is saturated while ρ_c keeps on increasing (region (iii) in Fig. 3). This is the region of high oxide thickness ($t_{ox} > 1.5$ nm). The saturation of J_o in this region is due to the suppression in the tunneling current for the minority carriers up to the limit at which the recombination through bulk defects or front surface dominates J_o. The minimum value of J_o in Fig. 3 is ~ 0.5 fA/cm^2 that corresponds to bulk recombination lifetime of 100 ms and front surface recombination velocity of 1 cm/s. The flow of majority carriers, on the other hand, continues to be dominated by the tunneling resistance due to which ρ_c continues to increase with increasing t_{ox}. From these trends, it can be observed that an optimal value of t_{ox} for poly-Si based contacts could be ~ 1.5 nm for which we can achieve the lowest value of J_o without a significantly large ρ_c. As we further increase t_{ox}, ρ_c increases without any suppression in J_o.

Interestingly, by using similar topology of POLO contacts, different groups report different values of J_o and ρ_c. While Gan and Swanson [18] report higher values of J_o for very low values of ρ_c, Peibst et al. [26] report high values of ρ_c. In this regard, the surface recombination (front or back) is one of the key parameters which can modulate J_o. Inset of Fig. 3 shows the effect of passivation at front contact on cell characteristics with t_{ox} variation. For the lowest value of J_o (0.5 fA/cm^2) in Fig. 3, value of v_{surf} at the top contact is 1 cm/s which corresponds to $D_{it} \sim 1 \times 10^8$ cm^{2}eV^{-1}. As we increase D_{it} (v_{surf}) of the top metal contact, the lowest value of J_o increases. A similar trend is observed in experimental data reported in [22], [26], [31].

We now consider the trends (in dark) for the variation of pinholes in the oxide layer. As shown in Fig. 4, D_{ph} is varied in the range of $\sim 10^7 - 10^{11}$ cm^{-2} for different cases of resistive and shorted pinholes, for a thick oxide ($t_{ox} = 3$ nm). As more and more pinholes are introduced in the oxide layer, charge carriers find increasing parallel paths of low resistance to flow through. Since majority (minority) carriers can flow easily through these parallel paths, ρ_c (J_o) decreases (increases). For very low D_{ph} ($\sim 10^7$ cm^{-2}), J_o is saturated to its lowest value because the oxide layer is nearly intact and the front surface recombination dominates J_o. For higher values of D_{ph} ($> 10^9$ cm^{-2}), J_o shows a higher sensitivity to D_{ph}. ρ_c shows a significant sensitivity for entire range of D_{ph} ($10^7 - 10^{11}$ cm^{-2}). Similar trends have been reported for analytical models in [40]. It is interesting to note that for low D_{ph} ($\sim 10^7$ cm^{-2}), J_o for shorted versus resistive pinholes is almost the same while their respective ρ_c shows a significant difference. This difference in ρ_c continues for the entire range of D_{ph}. Inset of Fig. 4 shows that as the pinhole acquires more and more resistance, due to increasing value of its residual oxide, we move toward the region of higher ρ_c and lower J_o. For the case of resistive pinholes, minimum value of resistance can only be achieved at very high D_{ph} ($> 10^{11}$ cm^{-2})—a situation when most of the oxide layer is broken-up with pinholes.

To demonstrate the effect of pinholes in thinner oxide layers, we study the pinhole variation for $t_{ox} = 1$ nm. For this case, ρ_c / J_o is almost constant for ($D_{ph} \leq 10^9$ cm^{-2}) and changes significantly for $D_{ph} > 10^{10}$ cm^{-2}, as seen in Fig. 5. Contact resistance is relatively unaffected for lower value of D_{ph} for the fact that majority carrier tunneling through the 1 nm is strong enough to offer a significantly low resistance to carrier

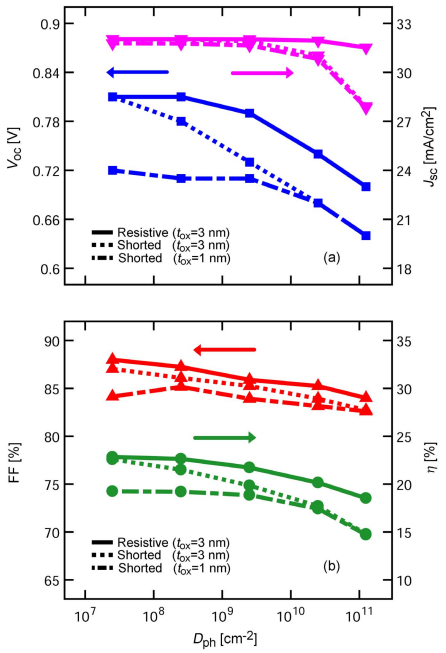

Fig. 7. Solar cell characteristics as a function of D_{ph} under illumination. For resistive pinholes, 0.3 nm of residual oxide is assumed to be present inside the pinhole region. v_{surf} for the front metal contact has been assumed to be 1 cm/s for all three cases.

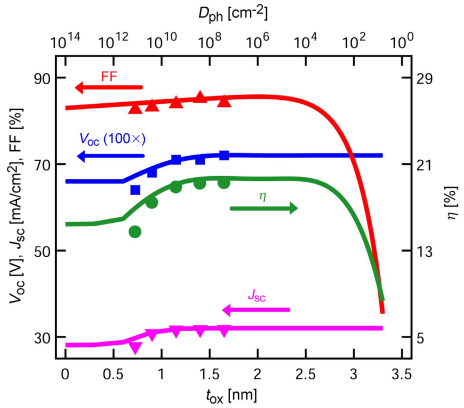

Fig. 8. Comparison of solar cell characteristics under illumination as a function of t_{ox} and D_{ph}. Solid lines are for t_{ox} variation while symbols represent variation in D_{ph} for shorted pinholes in thin tunneling oxide ($t_{ox} = 1$ nm).

flow. For higher D_{ph} ($> 10^{10}$ cm^{-2}), pinholes bring a modest decrease in the contact resistance.

A comparison of the effects of D_{ph} and t_{ox} variation on dark characteristics shows a close resemblance between the two trends. The results shown in Figs. 3 and 4 for $t_{ox} = 3$ nm are plotted together in Fig. 6. As the pinholes are introduced in the oxide (3 nm) at a very low density ($\sim 10^7$ cm^{-2}), the values for J_o and ρ_c become similar to that for $t_{ox} \sim 1.8$ nm (with no pinhole). A change in D_{ph} in the range of $10^7 - 10^{11}$ cm^{-2} at $t_{ox} = 3$ nm closely resembles to a change in t_{ox} (with no pinholes) from 1.8 nm to a very small value of oxide thickness ($\sim$ 0.6 – 0.7 nm).

B. Trends Under Light

The characteristics of the solar cell under illumination are shown in Fig. 7 for shorted and resistive pinholes for $t_{ox} = 3$ nm and 1 nm. Since standard AM1.5G solar spectrum is not available in PADRE, the light characteristic are obtained under uniform generation in the absorber and absolute values should, therefore, be understood only in the relative terms. Nevertheless, a reasonable insight into the general trends of the solar cell's performance under light can be obtained. Since J_o increases with an increase in D_{ph}, we see a degradation in efficiency (η) for higher D_{ph}. For the case of shorted pinholes in $t_{ox} = 3$ nm, open circuit voltage (V_{oc}) and efficiency significantly drop with an increase in D_{ph}. Short-circuit current density (J_{sc}), however, remains undisturbed for lower D_{ph} but slightly drops for D_{ph} ($>10^{10}$ cm^{-2}). Unlike thicker oxide ($t_{ox} = 3$ nm), the thinner oxide ($t_{ox} = 1$ nm) shows lower degradation in cell characteristics for shorted pinholes at low D_{ph} ($10^7 - 10^9$ cm^{-2}). For the case of resistive pinholes (solid curves), degradation with increasing D_{ph} is lower as compared to that for the shorted pinholes at the same t_{ox} (3 nm). The reason for this behavior is the additional blocking effect offered by the residual oxide present inside pinhole. Since higher values of D_{ph} can significantly degrade η, careful fabrication techniques that can minimize D_{ph} are desired.

Fig. 8 shows the cell characteristics as a function of t_{ox}. For $t_{ox} \geq 1$ nm, J_{sc} is slightly improved with increasing t_{ox} due to a decrease in tunneling probability for minority carriers through oxide barrier. V_{oc} also increases as t_{ox} is increased due to reduction of J_o. This behavior is analogous to the typical MIS solar cells. As t_{ox} is increased beyond 2.5 nm, characteristics start deteriorating due to the suppression of photogenerated carrier flux through a thick oxide barrier. The FF and efficiency, therefore, drop significantly.

Just like the case of solar cell characteristics under dark, we see a close resemblance between oxide and pinhole variation models for the cell characteristics under illumination as shown in Fig. 8. The effect of variation in D_{ph} in the range of $10^7 - 10^{11}$ cm^{-2} for $t_{ox} = 1$ nm can equivalently be obtained through t_{ox} variation in the range of 0.7 – 1.7 nm.

C. Comparison With Experimental Data

We now use our model to understand some of the trends in a set of reported experimental data. Fig. 9 shows a comparison of experimental data reported by various groups for

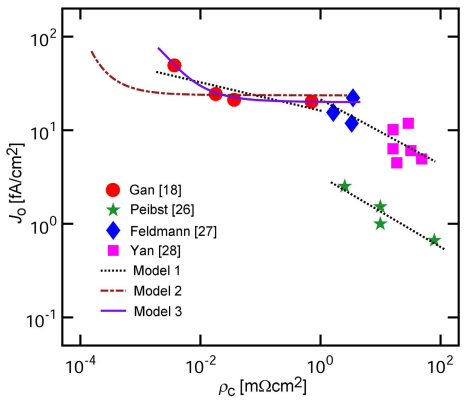

Fig. 9. Match with experimental data. Symbols represent the experimental data from different groups and lines represent our proposed models.

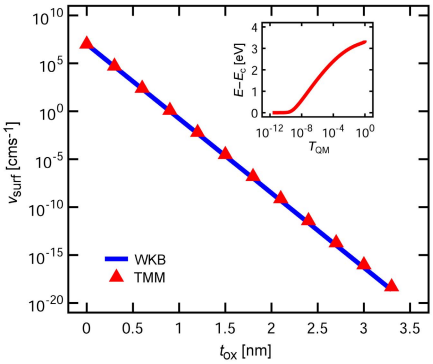

Fig. A1. Comparison of surface recombination velocity calculated through W-K-B approximation (line) and TMM (symbol). Inset shows a plot for T_{QM} versus $(E - E_c)$.

n^+ poly-Si/c-Si junctions (symbols), as well as simulation trends from our models. To interpret the set of experimental data, we use three different models. Model 1 is based upon coupled variation in t_{ox} and D_{it}. Model 2 is based upon variation only in t_{ox}. Model 3 is based upon variation of D_{ph} in the oxide. The experimental data from Gan *et al.* show trends which have a remarkably good match with model 3 where D_{ph} is varied in the range of $\sim 10^7 - 10^{10}$ cm^{-2}. Interestingly, Gan and Swanson [18] also predicted the formation of pinholes in oxide layer during the two-step annealing process in their work. To compare the same data with model 1, v_{surf} is varied in the range of 420 – 1000 cm/s and t_{ox} in the range of 1.5 – 2 nm which provides a linear curve not showing a good match with the data. For the data of Peibst *et al.*, model 1 shows a relatively good correlation by varying t_{ox} in the range of 2.2 – 2.8 nm along with variation of v_{surf} in the range of 4 – 40 cm/s. For the data from Feldmann *et al.* and Yan *et al.*, model 1 with t_{ox} variation of 1.7 – 2.2 nm, and v_{surf} of 70 cm/s and 400 cm/s, respectively, provides a good match with the trends. From these trends, we infer that for higher values of ρ_c, t_{ox} variation coupled with surface state variation (model 1) best explains the data. For the case of very low values of ρ_c, the effect of pinholes seems to be significant.

Although this paper has focused on symmetrically doped n-Si/n-poly contacts, the simulation framework used here can be applied to asymmetrically doped n-Si/p-poly contacts. The relative trends for symmetric versus asymmetric POLO contacts are intended to be explored as a part of a future study.

IV. Conclusion

We have performed a computational study to understand the relative effects of tunneling and pinholes in POLO contacts for crystalline silicon solar cells. The dark and light characteristics for these solar cells with varying pinhole density show a behavior similar to that for varying oxide thickness within an appropriate range. A comparison of our model with a set of experimental data suggests that pinhole transport may be dominant when contact resistance is very small ($< 10^{-1}$ mΩcm^2) and saturation current density is relatively large (> 10 fA/cm^2). The relative effect of pinholes strongly depends on the oxide thickness, with thicker oxides (≥ 2 nm) exhibiting a significant pinholes' effect. The qualitative understanding enabled through our simple 2-D model is useful for interpreting and predicting the underlying mechanisms involved in the experimental data.

TABLE I
Parameters Used for Solar Cell Simulations

	Emitter	Bulk	BSF
	c–Si	c–Si	Poly–Si
Thickness [nm]	300	2×10^5	20
N_A [cm^{-3}]	1×10^{19}	–	–
N_D [cm^{-3}]	–	1×10^{16}	1×10^{19}
τ [ms]	100	100	1×10^{-9}
μ_n [cm^2/Vs]	1000	1200	1000
μ_p [cm^2/Vs]	450	500	450
R_{an} [cm^6/s]	1.1×10^{-30}	1.1×10^{-30}	1.1×10^{-30}
R_{ap} [cm^6/s]	0.3×10^{-30}	0.3×10^{-30}	0.3×10^{-30}
N_c [cm^{-3}]	2.82×10^{19}	2.82×10^{19}	2.82×10^{19}
N_v [cm^{-3}]	1.83×10^{19}	1.83×10^{19}	1.83×10^{19}

$N_A(N_D)$: Doping, τ : Carrier lifetime, $\mu_n(\mu_p)$: Carriers mobility
$R_{an}(R_{ap})$: Auger recombination coefficient, $N_c(N_v)$: Density of States

Appendix

A. Quantum Mechanical Tunneling

T_{QM} calculated using TMM is shown in Fig. A1 (inset). The average transmission probability ($\langle T_{TMM}\rangle$) through the oxide barrier can be calculated by [49]:

$$\langle T_{TMM}\rangle = \int_{E_{min}}^{E_{max}} T_{QM}(E)\frac{df(E)}{dE}dE \tag{A1}$$

where $f(E)$ is the fermi function. $\langle T_{TMM}\rangle$ is then compared with the analytical tunneling probability ($\langle T_{WKB}\rangle$) calculated using W-K-B approximation [45]:

$$\langle T_{WKB}\rangle = e^{-\alpha\sqrt{\phi_{ox}}t_{ox}} \tag{A2}$$

where ϕ_{ox} is the original energy barrier for the carriers, α is the tunneling constant which depends upon carrier tunneling mass (taken to be 0.5 times the rest mass for electron [50]–[52]) in SiO_2 and t_{ox} is the oxide thickness, varied in range of 0 – 3.3 nm. For Si/SiO_2 contact, ϕ_{ox} for electrons and holes is 3.2 and 4.6 eV, respectively. Fig. A1 shows that $\langle T_{TMM}\rangle$ matches closely with $\langle T_{WKB}\rangle$.

B. Band Adjustment

In the simulations, the band bending is calculated through the coupled solution of electrostatic (Poisson) equation and charge density equations. Poisson equation at c-Si surface close to the back contact is given by:

$$\Delta^2 V(x,y) = \frac{\rho}{\epsilon_s} = \frac{q}{\epsilon_s}[N_D - n(x,y)] \tag{A3}$$

where $V(x,y) = -E_c/q$ is the electrostatic potential, E_c is the conduction band energy, ρ is the net charge density,

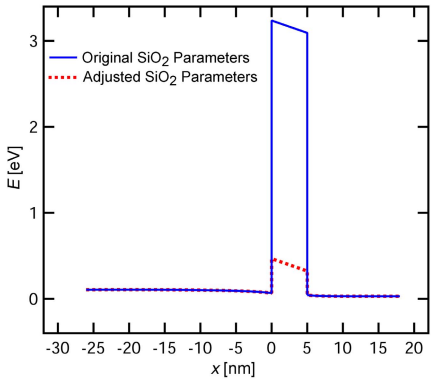

Fig. A2. Simulated conduction band profile for two different cases: i) with original parameters of SiO_2 and ii) adjusted values of bandgap and electron affinity in SiO_2. The SiO_2 thickness is 1.5 nm.

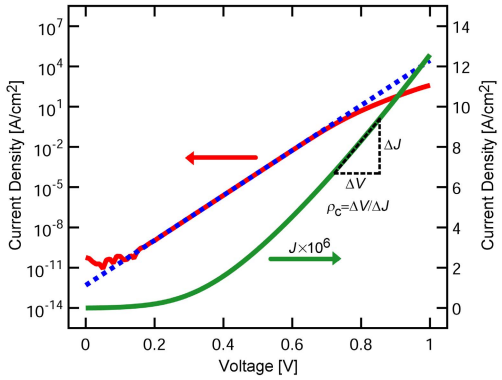

Fig. A3. Extraction of saturation current density J_o from simulated $ln(J) - V$ curve of the solar cell (plotted on left axis). Dotted blue line is the extrapolated y-intercept of the curve which gives us the value of J_o. Plotted on the right axis is the extraction of contact resistance ρ_c from simulated $J - V$ curve for the POLO contact. Slope of the curve gives us the value of ρ_c.

and N_D and $n(x, y)$ are the doping (includes in-diffusion from poly-Si) and electron densities, respectively. The charge density is given by:

$$n(x, y) = N_c F_{1/2}(E_c - F_n/k_B T) \tag{A4}$$

where N_c is the effective density of states (a material constant) for condition band, F_n is the quasi Fermi level for electrons, $F_{1/2}$ is the Fermi–Dirac integral of order 1/2, and $k_B T$ is the thermal energy.

Equations (A3) and (A4) are solved for a given set of boundary conditions which include the applied voltages and the continuity of currents at the contacts. Equations (A3) and (A4) imply that change in $V(x, y)$ or the band bending are directly related to $n(x, y)$. Hence, we need to ensure that the surface carrier density n_s at Si/SiO_2 interface does not vary while changing the bandgap (E_g) or electron affinity (χ) of SiO_2.

For a given set of applied conditions under a steady-state operation, n_s is a function of transmission probability through the oxide. As long as we satisfy (2) in our approach, transmission probability does not vary while changing the E_g or χ of SiO_2. As a result, n_s and, hence, the surface band bending remains independent to the changes in E_g and χ.

Fig. A2 shows the simulated conduction band diagram at the POLO contact with original E_g and χ of SiO_2. For comparison, conduction band diagram which incorporates adjusted values of E_g and χ of SiO_2 (while satisfying (2)) is plotted. It could be noted that bending in both cases matches nicely which validates the theoretical arguments provided in the above-mentioned discussion.

C. Calculation of J_o and ρ_c

J_o is extracted from simulated $ln(J) - V$ curve under dark. For ρ_c, we simulate only the POLO junction including the in-diffusion region in c-Si under oxide to avoid effects of bulk resistance. ρ_c is calculated by finding out the slope of $J - V$ curve at high bias (close to V_{oc}) as shown in Fig. A3.

D. 2-D Versus 3-D Crowding Resistance Effect

Since our 2-D model could underestimate the current crowding effects (see Fig. 1), we compare our simulated ρ_c and J_o values with those obtained through a widely accepted 3-D Fischer's model for a point-contacted solar cell [37], [42]

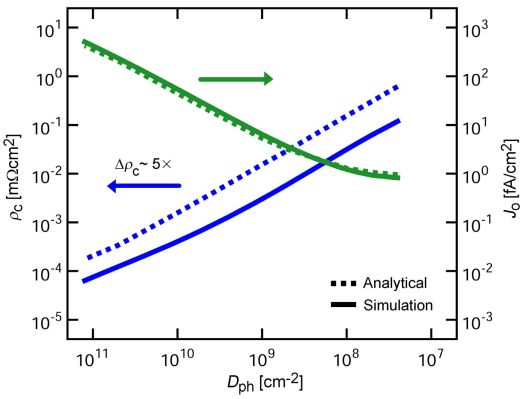

Fig. A4. Comparison of ρ_c and J_o as a function of D_{ph} calculated analytically (Fischer's model) and 2-D numerical simulations. Both models are in a good agreement for J_o. For ρ_c, the qualitative trend matches but the 3-D analytical values are $\sim 5\times$ higher as compared to 2-D simulations due to pinholes' crowding effect.

in Fig. A4. All physical parameters for the solar cell are kept similar for the comparison. While both models are in good qualitative agreement for ρ_c, a quantitative difference ($\Delta\rho_c$) of $\sim 5\times$ exists between the two approaches. We attribute it to the under-estimated crowding resistance in 2-D model and scale all simulated results for ρ_c with $5\times$ to incorporate the crowding effect. For J_o, 2-D versus 3-D models show a good match which implies that crowding effect is not substantial for J_o. This is because J_o includes the effect of the series resistance of thick base region which remains dominant over the crowding resistance for all D_{ph}.

REFERENCES

[1] S. Schäfer and R. Brendel, "Accurate calculation of the absorptance enhances efficiency limit of crystalline silicon solar cells with lambertian light trapping," *IEEE J. Photovolt.*, vol. 8, no. 4, pp. 1156–1158, Jul. 2018.

[2] M. A. Green, Y. Hishikawa, E. D. Dunlop, D. H. Levi, J. Hohl-Ebinger, and A. W. Ho-Baillie, "Solar cell efficiency tables (version 52)," *Progr. Photovolt.*, vol. 26, no. 7, pp. 427–436, 2018.

[3] Z. C. Holman *et al.*, "Current losses at the front of silicon heterojunction solar cells," *IEEE J. Photovolt.*, vol. 2, no. 1, pp. 7–15, Jan. 2012.

[4] J. Melskens, A. H. M. Smets, M. Schouten, S. W. H. Eijt, H. Schut, and M. Zeman, "New insights in the nanostructure and defect states of hydrogenated amorphous silicon obtained by annealing," in *Proc. IEEE 38th Photovoltaic Spec. Conf. (PVSC)*, Jun. 2012, pp. 1–8.

[5] J. Melskens, B. W. H. van de Loo, B. Macco, L. E. Black, S. Smit, and W. M. M. Kessels, "Passivating contacts for crystalline silicon solar cells: From concepts and materials to prospects," *IEEE J. Photovolt.*, vol. 8, no. 2, pp. 373–388, Mar. 2018.

[6] J. Schmidt, R. Peibst, and R. Brendel, "Surface passivation of crystalline silicon solar cells: Present and future," *Solar Energy Mater. Solar Cells*, vol. 187, pp. 39–54, Dec. 2018.

[7] H. Imran, T. M. Abdolkader, and N. Z. Butt, "Carrier-selective Nio/Si and Tio_2/Si contacts for silicon heterojunction solar cells," *IEEE Trans. Electron Devices*, vol. 63, no. 9, pp. 3584–3590, Sep. 2016.

[8] R. Islam, P. Ramesh, J. H. Nam, and K. C. Saraswat, "Nickel oxide carrier selective contacts for silicon solar cells," in *Proc. IEEE 42nd Photovoltaic Spec. Conf. (PVSC)*, Jun. 2015, pp. 1–4.

[9] C. Battaglia *et al.*, "Hole selective moO_x contact for silicon solar cells," *Nano Lett.*, vol. 14, no. 2, pp. 967–971, 2014.

[10] A. Savva and S. A. Choulis, "Cesium-doped zinc oxide as electron selective contact in inverted organic photovoltaics," *Appl. Phys. Lett.*, vol. 102, no. 23, 2013, Art. no. 233301.

[11] S. Avasthi, S. Lee, Y.-L. Loo, and J. C. Sturm, "Role of majority and minority carrier barriers silicon/organic hybrid heterojunction solar cells," *Adv. Mater.*, vol. 23, no. 48, pp. 5762–5766, 2011.

[12] S. Jäckle *et al.*, "Potential of PEDOT: PSS as a hole selective front contact for silicon heterojunction solar cells," *Sci. Rep.*, vol. 7, no. 1, 2017, Art. no. 2170.

[13] I. R. C. Post, P. Ashburn, and G. R. Wolstenholme, "Polysilicon emitters for bipolar transistors: A review and re-evaluation of theory and experiment," *IEEE Trans. Electron Devices*, vol. 39, no. 7, pp. 1717–1731, Jul. 1992.

[14] G. R. Wolstenholme, "An investigation of the thermal stability of the interfacial oxide in polycrystalline silicon emitter bipolar transistors by comparing device results with high-resolution electron microscopy observations," *J. Appl. Phys.*, vol. 61, no. 1, pp. 225–233, 1987.

[15] A. A. Eltoukhy and D. J. Roulston, "The role of the interfacial layer in polysilicon emitter bipolar transistors," *IEEE Trans. Electron Devices*, vol. ED-29, no. 12, pp. 1862–1869, Dec. 1982.

[16] J. S. Hamel, D. J. Roulston, C. R. Selvakumar, and G. R. Booker, "Two-dimensional analysis of emitter resistance in the presence of interfacial oxide breakup in polysilicon emitter bipolar transistors," *IEEE Trans. Electron Devices*, vol. 39, no. 9, pp. 2139–2146, Sep. 1992.

[17] F. A. Lindholm, A. Neugroschel, M. Arienzo, and P. A. Iles, "Heavily doped polysilicon-contact solar cells," *IEEE Electron Device Lett.*, vol. ED-6, no. 7, pp. 363–365, Jul. 1985.

[18] J. Y. Gan and R. M. Swanson, "Polysilicon emitters for silicon concentrator solar cells," in *Proc. IEEE Conf. Photovoltaic Spec.*, May 1990, pp. 245–250.

[19] P. Borden *et al.*, "Polysilicon tunnel junctions as alternates to diffused junctions," in *Proc. 23rd Eur. Photovoltaic Solar Energy Conf.*, Valencia, Spain, 2008, pp. 1149–1152.

[20] F. Feldmann, M. Bivour, C. Reichel, H. Steinkemper, M. Hermle, and S. W. Glunz, "Tunnel oxide passivated contacts as an alternative to partial rear contacts," *Sol. Energy Mater. Sol. Cells*, vol. 131, pp. 46–50, Dec. 2014.

[21] F. Feldmann, M. Simon, M. Bivour, C. Reichel, M. Hermle, and S. W. Glunz, "Carrier-selective contacts for Si solar cells," *Appl. Phys. Lett.*, vol. 104, no. 18, 2014, Art. no. 181105.

[22] A. Rohatgi, "Fabrication and modeling of high-efficiency front junction n-type silicon solar cells with tunnel oxide passivating back contact," *IEEE J. Photovolt.*, vol. 7, no. 5, pp. 1236–1243, Sep. 2017.

[23] F. Haase *et al.*, "Laser contact openings for local poly-si-metal contacts enabling 26.1%-efficient POLO-IBC solar cells," *Sol. Energy Mater. Sol. Cells*, vol. 186, pp. 184–193, Nov. 2018.

[24] H. C. Card and E. H. Rhoderick, "Studies of tunnel MOS diodes I. Interface effects in silicon Schottky diodes," *J. Phys. D, Appl. Phys.*, vol. 4, no. 10, p. 1589, 1971.

[25] H. Steinkemper, F. Feldmann, M. Bivour, and M. Hermle, "Numerical simulation of carrier-selective electron contacts featuring tunnel oxides," *IEEE J. Photovolt.*, vol. 5, no. 5, pp. 1348–1356, Sep. 2015.

[26] R. Peibst *et al.*, 'Working principle of carrier selective poly-Si/c-Si junctions: Is tunnelling the whole story?" *Sol. Energy Mater. Sol. Cells*, vol. 158, pp. 60–67, Dec. 2016.

[27] F. Feldmann *et al.*, "Advanced passivated contacts and their applications to high-efficiency cells," in *Proc. Workshop Crystalline Silicon Sol. Cells Modules*, Keystone, CO, USA, 2015.

[28] D. Yan, A. Cuevas, J. Bullock, Y. Wan, and C. Samundsett, "Phosphorus-diffused polysilicon contacts for solar cells," *Sol. Energy Mater. Sol. Cells*, vol. 142, pp. 75–82, Nov. 2015.

[29] D. Yan, "Heavily doped carrier-selective regions for silicon solar cells," Ph.D. dissertation, Dept. College Eng. Comput. Sci., Austral. Nat. Univ., Canberra, Australia, 2016.

[30] K. Lancaster, S. Großer, F. Feldmann, V. Naumann, and C. Hagendorf, "Study of pinhole conductivity at passivated carrier-selected contacts of silicon solar cells," *Energy Procedia*, vol. 92, pp. 116–121, Aug. 2016.

[31] U. Römer, "Polycrystalline silicon/monocrystalline silicon junctions and their application as passivated contacts for Si solar cells," Ph.D. dissertation, Univ. Hannover, Hanover, Germany, 2015.

[32] Römer, "Ion implantation for poly-Si passivated back-junction back-contacted solar cells," *IEEE J. Photovolt.*, vol. 5, no. 2, pp. 507–514, Mar. 2015.

[33] M. Rienäcker, "Junction resistivity of carrier-selective polysilicon on oxide junctions and its impact on solar cell performance," *IEEE J. Photovolt.*, vol. 7, no. 1, pp. 11–18, Jan. 2017.

[34] R. Peibst *et al.*, "A simple model describing the symmetric I–V characteristics of p polycrystalline Si/n monocrystalline Si, and n polycrystalline Si/p monocrystalline Si junctions," *IEEE J. Photovolt.*, vol. 4, no. 3, pp. 841–850, May 2014.

[35] T. F. Wietler, "Pinhole density and contact resistivity of carrier selective junctions with polycrystalline silicon on oxide," *Appl. Phys. Lett.*, vol. 110, no. 25, 2017, Art. no. 253902.

[36] Y. Zeng, "Theoretical exploration towards high-efficiency tunnel oxide passivated carrier-selective contacts (TOPCon) solar cells," *Solar Energy*, vol. 155, pp. 654–660, Oct. 2017.

[37] H. Plagwitz and R. Brendel, "Analytical model for the diode saturation current of point-contacted solar cells," *Prog. Photovolt., Res. Appl.*, vol. 14, no. 1, pp. 1–12, 2006.

[38] U. Römer, "Recombination behavior and contact resistance of n^+ and p^+ poly-crystalline Si/mono-crystalline Si junctions," *Sol. Energy Mater. Sol. Cells*, vol. 131, pp. 85–91, Dec. 2014.

[39] F. Feldmann, "A study on the charge carrier transport of passivating contacts," *IEEE J. Photovolt.*, vol. 8, no. 6, pp. 1503–1509, Nov. 2018.

[40] F. Feldmann *et al.*, "Charge carrier transport mechanisms of passivating contacts studied by temperature-dependent J-V measurements," *Sol. Energy Mater. Sol. Cells*, vol. 178, pp. 15–19, May 2018.

[41] N. Folchert, M. Rienäcker, A. A. Yeo, B. Min, R. Peibst, and R. Brendel, "Temperature-dependent contact resistance of carrier selective poly-Si on oxide junctions," *Sol. Energy Mater. Sol. Cells*, vol. 185, pp. 425–430, Oct. 2018.

[42] B. Fischer, "Loss analysis of crystalline silicon solar cells using photoconductance and quantum efficiency measurements," Ph.D. dissertation, Dept. Phys., Univ. Konstanz, Konstanz, Germany, 2003.

[43] R. F. Pierret and G. W. Neudeck, *Advanced Semiconductor Fundamentals*, vol. 6. Reading, MA, USA: Addison-Wesley, 1987.

[44] E. Yablonovitch, D. L. Allara, C. C. Chang, T. Gmitter, and T. B. Bright, "Unusually low surface-recombination velocity on silicon and germanium surfaces," *Phys. Rev. Lett.*, vol. 57, no. 2, p. 249, 1986.

[45] S. M. Sze and K. K. Ng, *Physics Of Semiconductor Devices*. Hoboken, NJ, USA: Wiley, 2006.

[46] M. R. Pinto *et al.* (Jan. 2006). *Padre*. [Online]. Available: https://nanohub.org/resources/padre

[47] T. M. Abdolkader, H. H. Hassan, W. Fikry, and O. A. Omar, "Solution of schrödinger equation in double-gate MOSFETs using transfer matrix method," *Electron. Lett.*, vol. 40, no. 20, pp. 1307–1308, 2004.

[48] T. M. Abdolkader, W. F. Farouk, O. A. Omar, and M. F. M. Hassan, "FETMOSS: A software tool for 2D simulation of double-gate MOSFET," *Int. J. Numer. Model., Electron. Netw., Devices Fields*, vol. 19, no. 4, pp. 301–314, 2006.

[49] D. Supriyo, *Lessons from Nanoelectronics: A New Perspective on Transport*. Trenton, NJ, USA: World Scientific, 2012.

[50] H. Watanabe, D. Matsushita, and K. Muraoka, "Determination of Tunnel Mass and Physical thickness of gate oxide including poly-Si/SiO_2 and Si/SiO_2 interfacial transition layers," *IEEE Trans. Electron Devices*, vol. 53, no. 6, pp. 1323–1330, Jun. 2006.

[51] D. König, M. Rennau, and M. Henker, "Direct tunneling effective mass of electrons determined by intrinsic charge-up process," *Solid-State Electron.*, vol. 51, no. 5, pp. 650–654, 2007.

[52] R. K. Chanana, "Determination of hole effective mass in SiO_2 and SiC conduction band offset using Fowler–Nordheim tunneling characteristics across metal-oxide-semiconductor structures after applying oxide field corrections," *J. Appl. Phys.*, vol. 109, no. 10, 2011, Art. no. 104508.